MATEC Web of Conferences **14**, 09004 (2014)
DOI: 10.1051/matecconf/20141409004

γ' precipitation kinetics in the powder metallurgy superalloy N19 and influence of the precipitation latent heat

Mikael Perrut[a] and Didier Locq

Onera – The French Aerospace Lab, 92322 Châtillon, France

Abstract. The N18 superalloy, powder metallurgy processed, is used for high-pressure turbine disks of the Snecma M88 engine and has been extensively studied. The size distribution of its γ' precipitates was first modelled in the late 1980's using a binary alloy model [1]. The precipitation model has been recently revised, upgraded in a pseudo-binary alloy model and used in a multi-scale mechanical model for the calculation of the fatigue life in low cycle fatigue conditions [2]. We here present how the new calibration of the pseudo-binary model for the N19 superalloy has been accelerated through the use of the Thermo-Calc® software, its TCNI5 thermodynamic database and its MOBNI2 mobility database. On a more fundamental point of view, the influence of the $\gamma > \gamma'$ latent heat of precipitation on the microstructural parameters of quenched samples of N18 and N19 has been studied using this same model. We conclude on the very importance of taking into account the latent heat in a coupled thermal-microstructural model for correct numerical simulations of the precipitation process at each point of a superalloy sample or part.

1. Introduction

Polycrystalline superalloys are widely used in the high temperature components of aeroengines. The powder metallurgy offers a better control of chemical segregation and grain size, giving opportunities for simpler numerical simulations of the precipitation process and the associated strengthening. This makes powder metallurgy polycrystalline superalloys good candidates for Integrated Computational Materials Engineering (ICME). World leading laboratories have been modelling the formation of γ/γ' microstructures in these alloys in order to quantitatively predict not only the microstructure but also the associated mechanical properties [3,4]. In this context, Onera is developing microstructural modelling in strong relationship with mechanical modelling. Successful results on the N18 γ/γ' superalloy have already been published [2].

The present paper shows how the N18 precipitation model has been modified for N19 superalloy. A Calphad-based calibration was performed in order to test the capability of the model to be directly adapted from one chemical composition to another. However, a particular point is stressed concerning the microstructural modelling of superalloys in general: the strong influence of the latent heat of precipitation makes it necessary to compute a fully-coupled thermo-microstructural evolution.

[a] Corresponding author: mikael.perrut@onera.fr

2. Precipitation model

2.1. Brief description of the precipitation model

Our precipitation model is based on N. Milhet-Gayraud PhD work [1] with recent modifications carried out by G. Boittin [2]. This model is now implemented in Z-set software [5]. We remind here shortly the approach, the main assumptions and the input parameters associated to the model. This is a class model, based on classical nucleation and LSW coarsening theory, where precipitates are distributed in classes of size. It calculates the size distribution of intragranular γ' precipitates over the time, depending on the material thermal history (which is supposed to be given as an input of the model). The obtained distribution is most of the time bimodal or even n-modal ($n > 2$). It results in the knowledge of relevant parameters for the microstructure at the end of the heat treatment: mean sizes and volume fractions of each mode of the distribution (i.e. secondary and tertiary γ' precipitates for $n = 2$). Primary precipitates do not interact directly with the calculated intragranular precipitation, but their existence strongly modifies the matrix chemical composition inside the grains, which is taken into account in the model.

As this kind of calculation is performed at each Gauss point of a mesh, it is necessary to simplify the problem. It is therefore assumed that: the precipitates are isolated spheres (no interaction between precipitates), the influence of elasticity is neglected, the precipitate/matrix interfaces are at local equilibrium. A pseudo-binary approach is used to calculate the equilibrium concentrations: the Al, Ti and Nb γ'-forming element concentrations are summed to

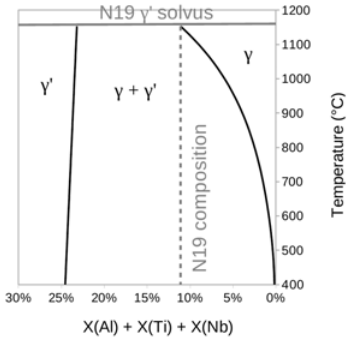

Figure 1. Pseudo-binary phase diagram of the N19 alloy obtained by Thermo-Calc software. The isopleth projection is built by summing the molar fractions of Al, Ti and Nb γ'-forming elements.

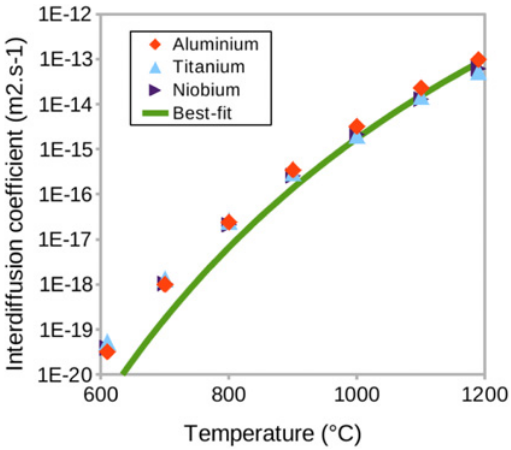

Figure 2. Interdiffusion coefficients of Al, Ti and Nb in the N19 γ phase for various temperatures (results obtained with the Dictra software), compared with our effective diffusion coefficient which better fitted experimental results.

deduce a "solute" concentration, like in the PhD work of J. Mao [6]. A single "effective" energy-activated diffusion coefficient is used to match the precipitation kinetics. The driving force is taken from [7] and consists in a simple analytical expression of the matrix supersaturation and is not specific to the material.

The list of the material-dependent input parameters is: initial solute concentration, interfacial energy, pseudo-binary phase diagram, effective diffusion coefficient and its activation energy, volume fraction of primary γ' precipitates. The molar volume of the γ' phase is also needed but its slight variation has only little impact on the kinetics as elasticity influence is not taken into account. The interfacial energy is assumed to be constant, whatever the temperature or the size of the precipitates. This simple model has few material-dependent input parameters, but it was successfully used to describe N18 precipitation kinetics. However, it was time consuming to determine experimentally the pseudo-binary phase diagram. It was then decided to test, for the calibration of N19 precipitation kinetics, a Calphad-based calibration with even fewer experiment-based input parameters.

2.2. Calphad-based calibration for the N19 precipitation model

The N19 precipitation model was calibrated thanks to a Calphad approach using Thermo-Calc (version S) and Dictra softwares (version 26) with, respectively, TCNI5 and MOBNI2 database for the determination of both the N19 pseudo-binary phase diagram and an effective diffusion coefficient [8–10]. Figure 1 shows the obtained phase diagram and Fig. 2 shows the diagonal interdiffusion coefficients for Al, Ti and Nb elements in the γ phase at its temperature-dependent equilibrium composition. It must be noticed that no coupling between Thermo-Calc (or Dictra) and Z-set is performed, but only *a priori* calculations for the input parameters.

The obtained phase diagram allows the calculation of polynomial fits of the evolution of the equilibrium molar fractions in γ'-forming elements of the γ phase and of the γ' phase from room temperature up to the calculated γ' solvus temperature (1153 °C). There is no need to optimize these calculated fractions. Concerning diffusion coefficients, it could be noticed that the three investigated elements have similar diffusion coefficients, which simplifies the problem very much. However, we had to optimize the effective diffusion coefficient by comparison with our experimental results. Calculated interdiffusion coefficients give a good initial estimate, especially at high temperature, but the activation energy has to be taken slightly higher to fit the experimental values of the precipitate mean sizes.

The last input parameter that strongly influences the precipitation kinetics is the energy of the $\gamma - \gamma'$ interface. It was determined by fitting the experimental results while keeping it in a relevant range (1 to 100 $\mathrm{mJ \cdot m^{-2}}$).

2.3. Latent heat introduction in the model and subsequent coupling

One issue of the present model is the assumption that the thermal history is given, and that precipitation does not affect the local temperature evolution. The early stages of precipitation are very impressive because large volumes of γ' phase form suddenly: the high nucleation rates can lead to a rise in precipitated volume fraction of more than $1\% \cdot \mathrm{s^{-1}}$. It was thus decided to take the latent heat of precipitation into account. A source term P is introduced into the heat Eq. (1):

$$\rho C_p \frac{\partial T}{\partial t} = \lambda \Delta T + P \quad \text{with} \quad P = \rho L \frac{\partial f_p}{\partial t} \qquad (1)$$

where ρ is the density of the alloy (assumed to be constant), c_p the heat capacity, λ the thermal conductivity and L the latent heat of transformation. As the latent heat of γ to γ' transformation is typically around $120\,\mathrm{kJ \cdot mol^{-1}}$ [11] (which has been experimentally checked for both N18 and N19 superalloys), this should produce a precipitation-induced local heating at an approximate rate of $2\,\mathrm{K \cdot s^{-1}}$, which is a typical cooling rate in the bulk part of a disk.

The precipitation latent heat automatically impacts the disk cooling kinetics and so the precipitation kinetics. Reciprocally, at each time step, the calculated

Table 1. Chemical compositions (at. %), γ' solvus temperature and typical γ' fraction at room temperature of N18 and N19 alloys.

at.%	Ni	Cr	Co	Mo	Ti	Al	W	Nb	Zr	Hf	B	C	γ' solvus	γ' frac.
N18	bal.	12.3	14.8	3.8	5.1	9.1	/	/	.018	.16	.083	.075	1195° C	55–60%
N19	bal.	14.6	12.0	2.9	4.6	5.5	1.0	1.0	.038	.1	.08	.1	1145° C	40–45%

microstructure evolution gives the new instantaneous volume fraction time derivative. Our model becomes a fully-coupled thermal-microstructural transient calculation. Numerically, both problems (the thermal one and the microstructural one) are solved at each time step, with a partitioned coupling technique [12]. The coupling is performed at each time step. Z-set software uses MPI [13] to synchronize and exchange data between its solvers, simply passing the source term P value (resp. temperature value) for each gauss point of the mesh from the microstructural (resp. thermal) problem to the thermal (resp. microstructural) problem.

Then, the algorithm chooses the next time step by taking the minimum of the two time steps, so that the two problems are fully synchronized without any risk of calculation divergence. This is an original way of choosing the next time step, adapted from earlier work at Onera [14]. It is highly important because the latent heat effect is relevant at the early stages of nucleation, which should be captured with a very short time step. On the other hand, at low temperature, the microstructure does not evolve any more, but a reasonably short time step is still required to ensure convergence of the calculated thermal evolution. Finally, the coupling additional cost in terms of CPU time is kept small compared to the CPU time needed for both problems when solved separately.

3. Experimental procedures

3.1. Materials

For this precipitation kinetics study, two alloys were used: N18 and N19. These are both powder metallurgy (PM) nickel-based superalloys developed for disk applications. N18 alloy is used for the manufacturing of the high-pressure compressor or turbine disks of the Snecma M88 engine [15,16]. N19 alloy is a recently developed disk superalloy with equivalent or higher mechanical properties and lower γ' fraction and solvus temperature than those of N18 alloy [17]. For these two materials, the same PM route is followed: argon atomization, sieving, hot isostatic pressing, extrusion (Aubert&Duval) and finally isothermal forging (Snecma). The typical chemical compositions of the alloys are presented in Table 1.

3.2. Experimental conditions

Several types of experiments were performed. First, a series of experiments for the determination of the mean size of γ' precipitates in N19 specimens. Laboratory samples (diameter of 12 mm and length of 20 mm) were all cut in a tangential direction from the rim of as-forged parts. These cylindrical specimens were heat-treated at a subsolvus (1120 °C/4 h) or supersolvus temperature (1180 °C/2 h), then cooled at a constant cooling rate from 10 to 400 $\mathrm{K \cdot min^{-1}}$ in special furnaces at the Centre des Matériaux [18]. For microstructural characterizations, the heat-treated specimens were radially half-length cut, then polished (diamond 1/4 μm) and chemically etched to reveal the γ' precipitation (glyceregia etchant). These observations were conducted on a Zeiss DSM982 Gemini scanning electron microscope (SEM). High magnification images (20 k–50 k range) were taken at the center of the specimen to avoid near-surface precipitation evolution.

3.3. Image analysis and microstructural parameters quantification

Image analysis was performed by using ImageJ software [19]. Images were smoothed and automatic thresholds were calculated [20]. Due to huge differences in the microstructures, it was not possible to use the same automatic image treatment for all microstructures. Below 50 $\mathrm{K \cdot min^{-1}}$, a special image treatment was designed for coarse secondary γ' precipitates. The latter have irregular morphologies, so that a cross-section imaging makes a single precipitate appear as several precipitates. This was corrected by using a special filter taking into account not only the pixel value but also the image local variance. The surface fraction was easily determined. The equivalent sphere radii were converted from area measurement of each particle. A size distribution is obtained, based on at least 250–500 counted particles. To each class of the radius distribution corresponds a number of precipitates but also a γ' volume fraction. The "precipitates mean size" corresponds to the average of the class radii, weighted with their corresponding γ' volume fraction. The same averaging method is implemented in our precipitation model, so that the compared values do definitely have the same physical meaning.

4. Experimental results and comparison with the numerical simulations

4.1. Mean sizes of precipitates in N19 samples after controlled cooling

Using Calphad-based input parameters makes the calibration of the model for N19 superalloy easy and fast. Even the effective diffusion coefficient had only to be modified at low temperatures. The validation of this approach was carried out by comparison with experimental mean sizes of secondary precipitates and corresponding surface fractions. Micrograph examples are shown in Fig. 3, where the microstructures are very different due to the variation in the applied cooling rates.

There was a very satisfying agreement between calculations and experimental results, as proved by Fig. 4, for both subsolvus and supersolvus heat treatments. The agreement is also good when comparing experimental surface fractions of the γ' phase and the calculated ones. In the case of subsolvus heat treatment, the primary

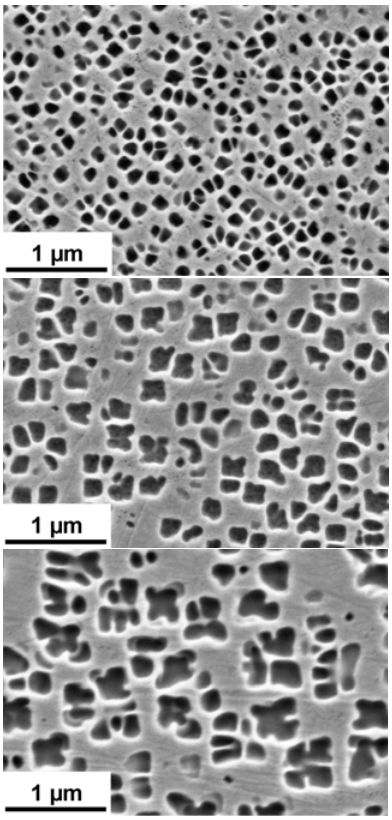

Figure 3. SEM micrographs showing the γ' secondary precipitates of N19 samples depending on the cooling rate.

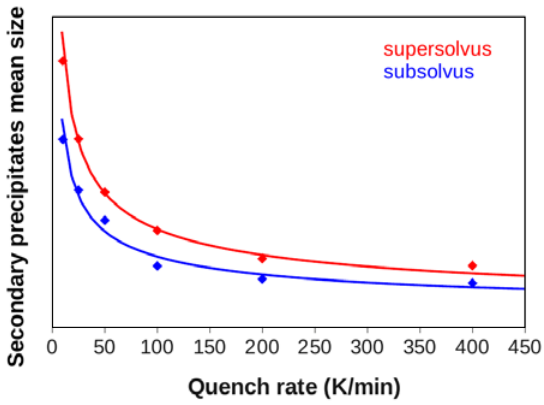

Figure 4. Comparison between experimental points and calculated curves of secondary precipitates mean sizes for subsolvus or supersolvus heat treatments according to the cooling rate.

precipitates volume fraction was experimentally estimated at a value of 10%, which was in agreement with the Calphad-based phase diagram. However, due to the control of the quench rates, the cooling is not a "natural" one, and the effect of latent heat is hidden by the furnace servocontrol. When considering an air cooling or oil quenching, the effects of the latent heat of precipitation will not be counteracted, and this must be taken into account.

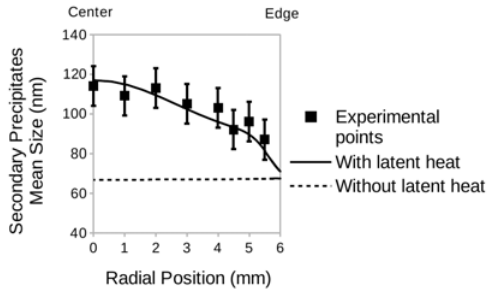

Figure 5. Comparison between experimental and calculated values of secondary precipitate mean sizes along the radius of a N19 cylindrical sample.

4.2. Microstructural gradient in a N19 cylindrical sample

The impact of the latent heat on the microstructure has been studied through a simple experiment on one of the N19 cylindrical samples. This sample was heated at 1200 °C (supersolvus) and air cooled, then radially half-length cut like the other samples. The microstructural characterization was performed not only at the center of the circular section but also along a radial axis. A microstructural gradient was observed: the secondary precipitates were slightly finer and the tertiary precipitates disappeared when the region of interest moved from the center towards the edge. The secondary precipitates became very much finer near the edge.

These features are well reproduced by our calculation, the agreement on the secondary precipitate sizes are shown in Fig. 5, when taking a value of $220\,\mathrm{W \cdot m^{-2} \cdot K^{-1}}$ for the convective heat transfer coefficient h. Even large variations of the h coefficient do not change the shape of the microstructural gradient, nor with neither without latent heat. Tertiary precipitation kinetics is even much more impacted than the secondary precipitation kinetics. However, as it is difficult to quantify the tertiary precipitates due to their small size, these modifications have not yet been studied.

On the other hand, the calculated thermal evolutions are very similar, considering the small size of the sample (12 mm diameter). The impact on the microstructures is tremendous compared to the slight changes in temperature evolutions. These evolutions are shown in Fig. 6, after that they have been shifted in time (by approximately 1s) in order to compare them better. Without latent heat, it is nearly impossible to distinguish any difference between the cooling at the center and the cooling at the edge of the sample above 800 °C. This explains why, in this case, the calculated precipitate mean sizes are independent of the location in the sample (Fig. 5). In order to highlight the impact of the latent heat, the time derivative of the temperature is also plotted in Fig. 6. Only the early stages of the cooling are plotted: this is the most relevant time range, because the nucleation is very strong and makes the latent heat effect visible. There is a systematic inflexion point in the thermal evolution at the onset of precipitation, resulting in a remarkable cusp when plotting the temperature time derivative *vs* temperature. It may be noticed that a second cusp (much smaller) is also visible

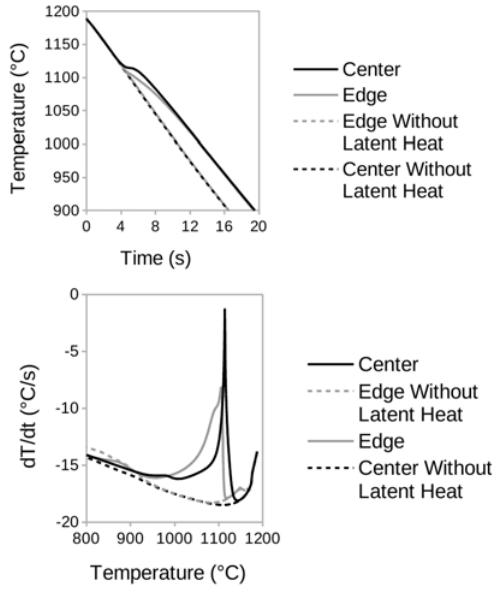

Figure 6. Impact of the latent heat on the calculated thermal evolutions (up: T; bottom: $\mathrm{d}T/\mathrm{d}t$), at the edge (grey) or in the center (black) of a N19 cylindrical sample.

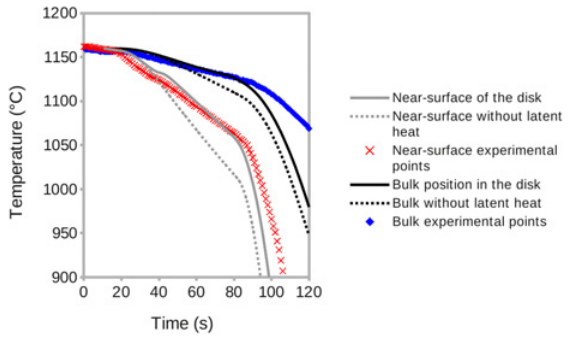

Figure 7. Calculated thermal evolutions inside a N18 disk during cooling; comparison with experimental points.

around 1000 °C in the calculated evolution for the center of the sample, corresponding to the nucleation of tertiary precipitates.

4.3. Thermal evolutions in a N18 disk

Temperature measurements were performed thanks to thermocouples placed on various locations in a N18 disk during an industrial-type cooling. Figure 7 shows the evolution of the measured temperature with time during the two first minutes of the cooling. It compares two different locations in the disk: a near-surface position (in a thin part of the disk, and only 1 mm from the surface) and a bulk position (in a massive part of the disk, 2 mm from the surface). There is no physical fitting parameter in the thermal problem since the convective heat transfer coefficients are calibrated by special industrial know-how, and since latent heat is still fixed at the value of 120 kJ·mol^{-1}.

Figure 8 shows that the cusp in the curve of the time derivative of the temperature is an experimental fact, even in industrial processing conditions. In addition, the

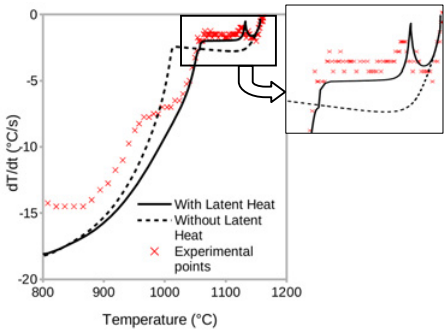

Figure 8. Calculated cooling rate evolution in a near-surface location of the disk; comparison with experimental points. The inset details the high temperature range of the curve.

agreement is good between experiment and calculation, without any fit.

Even in an industrial part, the latent heat allows to reproduce more correctly the thermal evolutions, namely the sudden variations of temperature at the onset of precipitation. This is beyond the scope of this article to describe in details the impact of the latent heat in the disk microstructure, but it is as strong in a massive sample as in a 12 mm sample.

5. Conclusion

A precipitation model, originally built for N18 superalloy, was modified for N19 superalloy. A Calphad approach was used for the calibration of the following input parameters: pseudo-binary phase diagram and effective diffusion coefficient. The experimental secondary precipitate mean sizes in the N19 superalloy were reproduced by the model with a very good agreement. The impact of the latent heat on the precipitation kinetics was pointed out: the variations of the mean size inside an air cooled N19 superalloy 12 mm sample were successfully explained by a strong coupling between the thermal evolution and the microstructural evolution. It has been stressed that such a coupling also occurs in industrial parts, and should definitely be taken into account. The agreement for the secondary precipitates is now very satisfying, and could not be improved that much. In order to go further in the improvement of the precipitation model, it is needed to study quantitatively the tertiary precipitates. This would give insights for the nucleation and coarsening at lower temperatures, with potential issues concerning the influence of elasticity.

This work was supported by the French Ministry of Defence (DGA). We thank Jean-Michel Franchet (Snecma) for the collaborative work and for the material supply. We thank Loïc Nazé (MINES ParisTech, Centre des Matériaux) for the special heat treatments, Catherine Ramusat (Onera) for metallography, Jean-Didier Garaud (Onera) for Z-set coupling implementation.

References

[1] N. Milhet-Gayraud, PhD thesis, Institut National Polytechnique de Grenoble, France (1994)

[2] G. Boittin, D. Locq, A. Rafray, P. Caron, P. Kanouté, F. Gallerneau, G. Cailletaud, in *Superalloys 2012*, edited by E.S. Huron et al., TMS, Warrendale, USA, 167–176 (2012)
[3] T.P. Gabb, D.G. Backman, D.Y. Wei, D.P. Mourer, D. Furrer, A. Garg, D.L. Ellis in *Superalloys 2000*, edited by T.M. Pollock et al., TMS, Warrendale, USA, 405–414 (2000)
[4] G.B. Olson, H.J. Jou, J. Jung, J.T. Sebastian, A. Misra, I. Locci, D. Hull, in *Superalloys 2008*, edited by R.C. Reed et al., TMS, Warrendale, USA, 923–932 (2008)
[5] Z-set / Zébulon, Material and structure analysis suite (2011), http://www.zset-software.com/
[6] J. Mao, PhD thesis, West Virginia University (2002)
[7] H. Wendt, P. Haasen, Acta Metall. Mater. **31–10**, 1649–1659 (1983)
[8] J.O. Andersson, T. Helander, L. Höglund, P.F. Shi, B. Sundman, Thermo-Calc and DICTRA, Computational tools for materials science. Calphad, 26, 273–312 (2002)
[9] Thermo-Calc Software TCNI5, March 2011
[10] Thermo-Calc Software MOBNI v2.4, Sept. 2012
[11] P.N. Quested, R.F. Brooks, L. Chapman, R. Morrell, Y. Youssef, K.C. Mills, Mater. Sci. Tech. **25-2**, pp.154–162 (2009)
[12] C.A. Felippa, K.C. Park, C. Farhat, Comput. Methods Appl. Mech. Engrg. **190**, 3247–3270 (2001)
[13] http://www.open-mpi.org/
[14] J.-D. Garaud, PhD thesis (chap. 3), Université Pierre et Marie Curie, Paris (2008)
[15] J.-Y. Guédou, J.-C. Lautridou, Y. Honnorat, in *Superalloys 1992*, edited by S.D. Antolovich et al., TMS, Warrendale, USA, 267–276 (1992)
[16] G. Raisson, J.H. Davidson, in *High Temperature Materials for Power Engineering*, edited by E. Bachelet et al., Kluwer Academic Publishers, Dordrecht, Netherlands, 1405–1416 (1990)
[17] J.-Y. Guédou, I. Augustins-Lecallier, L. Nazé, P. Caron, D. Locq, in *Superalloys 2008*, edited by R.C. Reed et al., TMS, Warrendale, USA, 21–30 (2008)
[18] A. Dumont, PhD thesis, École nationale supérieure des mines de Paris (2013)
[19] http://imagej.nih.gov/ij/index.html
[20] http://fiji.sc/wiki/index.php/Auto_Threshold